Enhancing the methanol yield of industrial-scale fixed bed reactors using computational fluid dynamics models

Stylianos Kyrimis, Robert Raja, Lindsay-Marie Armstrong

Abstract

Achieving our decarbonisation goals for the maritime transport sector requires the bulk production of liquid hydrocarbon fuels, suitable for the existing infrastructure, such as methanol (MeOH). For this, optimisation of fixed bed chemical reactors is vital. Unlike demonstration-scale setups, optimising the design of such reactors using Computational Fluid Dynamics (CFD) models is both cheaper and faster. In this study, using a 2D pseudo-homogeneous CFD model, a single tube from a multi-tubular industrial-scale MeOH reactor is simulated. Using available experimental data, the CFD model was validated yielding excellent accuracy, with an average error of 2.6%. The model identified a temperature hot-spot near the bed entrance, while the predicted pressure drop was 11% of the operating pressure. Both effects could considerably reduce the efficiency of the reactor, either by catalyst deactivation or by increasing the compressor requirements, respectively. Through a parametric study where the tube's length and diameter were varied within the ±50% range, 53 total cases are produced and solved, creating an extensive pareto set of data for the key output parameters, such as methanol production, pressure, and temperature. A response surface was also generated, revealing the interconnection between the tube's design and the operating parameters. This enabled a performance optimisation of the reactor design for two industrially relevant scenarios, with the optimised reactor achieving a 6.9% higher MeOH yield and a 75% reduced pressure drop. Through industrial involvement, the reactor can be further optimised, and would act as a critical foundation for more extensive techno-economic and socio-economic evaluations for sustainable carbon-neutral methanol production.

Keywords

Computational Fluid Dynamics (CFD), methanol (MeOH), reactor optimisation, decarbonisation, heterogeneous fixed bed catalytic reactors.

Introduction

As one of the most energy-efficient modes of transport, maritime transport plays a key role in the global economy, being responsible for over 80% of volume of global trade [1, 2]. Due to its dependence on fossil fuels, the greenhouse gas emissions of maritime transport reached 706 Mt of CO_2 in 2022 [3], with the International Maritime Organization (IMO) predicting further emissions growth by up to 250% by 2050 [4]. Such an increase is alarming, especially considering the urgency to achieve our climate goals and to not exceed the global warming threshold of 1.5 ^{o}C set by the Intergovernmental Panel on Climate Change (IPCC) report of 2018 [5]. While electrification could considerably reduce the emissions of urban vehicles [6-9], it is not directly applicable to heavy-duty road transport, maritime transport, or aviation [4]. Consequently, alternative strategies are required, such as the replacement of the currently used fossil fuels with carbon-neutral alternatives. Methanol (MeOH) is considered a promising candidate, being directly integrable in the existing fuel transportation and storage infrastructure [10, 11]. Moreover, methanol can act as a convenient storage and transportation solution for hydrogen applications, whilst also being a highly valuable building block for the chemical industry [12, 13]. Its importance and flexibility led Olah to suggest the methanol economy concept [14], with methanol playing a vital role in a sustainable and carbon-neutral society.

Methanol is synthesized from synthesis gas, i.e., a mixture of CO_2, CO, and H_2, making it a very attractive option for Carbon Capture and Utilisation (CCU) applications [15]. However, large-scale methanol production is currently dominated by fossil fuels, with natural gas acting as the primary feedstock for the supply of synthesis gas through steam reforming or autothermal reforming [13, 16]. The standard catalyst for methanol synthesis since 1970 has been the $Cu/ZnO/Al_2O_3$, with Cu ranging

from 20% to 80%, ZnO ranging from 15% to 50%, and Al_2O_3 ranging from 4% to 30% [12, 17]. Three competing pathways are involved in methanol synthesis from CO_2, CO, and H_2, the direct CO_2 hydrogenation reaction, R_1, the water-gas shift reaction, R_2, and the CO hydrogenation reaction, R_3. All three reactions are equilibrium-based, and their equilibrium dictates the final MeOH formation. The reactor is usually operated at a temperature range of 200-300 ^oC and a pressure range of 40-120 bar [17], with the maximum MeOH formation achieved at low temperatures and high pressures [17].

Despite the wide literature available, a clear consensus on the relative contribution of these three reactions has not been reached. Specifically, one of the first kinetic models (KM) available in the literature, that of Graaf *et al.* [18, 19], considers all three pathways to contribute to MeOH synthesis. Following the same school of thought, Park *et al.* [20] more recently developed their own KM, based on three active sites, a Cu^0 site where CO_2 is adsorbed, a Cu^+ site where CO is adsorbed, and a ZnO site where H_2 and H_2O are competitively adsorbed. On the contrary, isotope labelling studies concluded that MeOH is mainly produced from CO_2, while CO hydrogenation, R_3, is comparatively small [21-23]. This led to the development of KMs that excluded CO hydrogenation entirely, such as the KM of Bussche and Froment [24] and of Nestler *et al.* [25]. In our previous work [26], we compared the MeOH synthesis results produced from the KMs of Park *et al.* [20] and of Nestler *et al.* [25], as those were two of the latest models produced, i.e., at 2014 and at 2020, respectively. It was identified that while both KMs produced very accurate results, they resulted in unique species interactions and profiles through the catalytic bed [26]. Most notably, Park's KM predicted that for low CO concentrations in the feed, MeOH reverted back to CO, while a backwards reaction rate was never observed with Nestler's KM [26]. The development of both KMs was based on the experimental results of Park *et al.* [20], where a laboratory-scale MeOH synthesis reactor was used. Due to the small size of their reactor, being in the cm-scale, the temperature could be accurately controlled, and near-isothermal conditions could be achieved. However, in their subsequent study, Nestler *et al.* [27] argued that for industrial-scale reactors, being in the m-scale, accurate temperature control is more challenging and could lead to non-isothermal conditions which will affect local reaction kinetics. Consequently, they redefined

the constants of their KM by collecting results with a mini-plant reactor, having a length of 1.12 meters [27], making their adapted KM suitable for simulations of industrial-scale reactors.

Increasing the cost-competitiveness of carbon-neutral MeOH is key for its wide-scale deployment as a replacement for fossil fuels, and techno-economic analyses of industrial-scale plants, coupled with CCU-applications, have identified the key-economic drivers of the process [15, 28-31]. Specifically, one of the most expensive Capital Expense (CapEx) to build the MeOH synthesis system is the compressor, necessary to achieve the high-pressure required and drive the reactants through the bed [15]. H_2 production, produced through H_2O electrolysis, is the major Operating Expense (OpEx) [15, 28], with the cost of the catalyst being comparatively low and equal to 0.5% of total OpEx [31]. The primary revenue of the MeOH synthesis plant is MeOH, contributing by 71% of total profits. Secondary revenues are oxygen, contributing by 17%, and district heating, contributing by 12% [31]. Higher $CO_{2\text{-}eq}$ consumption for the plant can generate CO_2 credits, which can be traded in the market and act as an alternative revenue source [29, 30]. The generation of CO_2-credits is a cornerstone of the EU's policy against climate change [32] and has generated 42 million U.S. dollars in revenue in 2022 [33]. With the prices of CO_2 certificates expecting to increase further, production of more CO_2-credits from the MeOH synthesis plant can potentially generate a significant income [30]. Such techno-economic studies can act as guidelines for the goal-driven optimisation of the MeOH synthesis reactor. While most studies agree that H_2 generation and the electricity cost of the electrolyser is the key driver of the carbon-neutral MeOH sell price, this goes beyond the scope of this study. This is because H_2 production takes place ex-situ, and its production and cost are not associated with the reactor design, operation, and optimisation, i.e., the optimisation of the reactor for maximising MeOH synthesis will not affect the cost of H_2 production through electrolysis and vice-versa. However, the reactor is the primary driver of MeOH production, and optimising its design and operation to maximise MeOH yield can benefit both the plant revenue and the price of MeOH, making it more cost competitive.

Industrially, as highlighted by Bozzano and Manenti [12] and by Bisotti *et al.* [34], there are several MeOH reactor types commercially used [16, 35, 36], such as the low-pressure quench converter of Johnson Matthey [37], the water-cooled Lurgi-type reactor of Mega-Methanol [38], and the adiabatic reactor of Haldor Topsøe [16]. Being commercial applications, available data for these reactors are scarce in the literature. However, the in-house industrial-scale Lurgi-type reactor of Shiraz petrochemical in Iran has become one of the most widely studied reactors in the literature, given the availability of experimental data [25, 27, 39-52]. The baseline concept of Lurgi-type reactors [16] involves the $Cu/ZnO/Al_2O_3$ catalyst being loaded into long tubes, forming a fixed bed system where the catalyst remains immobile. The reactants flow through the interparticle pores formed by the final particle position, with the local bed structure affecting the flow path, velocity, and pressure drop of the flow field [53-55]. Moreover, the reactants can diffuse within the catalytic particles and react, forming MeOH. To control the operating temperature, water flows through the outer tube shell thus removing the heat produced from the exothermic MeOH synthesis reactions [46, 48]. The Shiraz petrochemical reactor consists of 2962 catalyst tubes, each with a length of 7.022 m and an inner diameter of 3.8 cm [45]. Moreover, detailed inlet and outlet composition information has been published, which will be presented in the following section.

Irrespective of its design, the MeOH synthesis reactor has some operating principles that it needs to adhere to. Apart from controlling the reaction kinetics, excessive reactor temperatures above 300 ^{o}C can sinter the $Cu/ZnO/Al_2O_3$ catalyst, leading to rapid deactivation [39, 46, 56]. On the other hand, if the temperature drops below 125 ^{o}C [41], condensation of MeOH and of H_2O could take place, which are a major concern for catalyst deactivation [41-43]. Finally, an excessive pressure drop along the reactor's length has a negative impact on the driving force of the reactions [46], while also considerably increasing CapEx and OpEx [57]. With the need to understand and optimise the behaviour of the MeOH synthesis reactor, literature studies have developed several computational models. Mirvakili *et al.* [42] performed 3D Computational Fluid Dynamics (CFD) simulations of an industrial-scale Lurgi-type MeOH synthesis reactor, revealing the heterogeneous flow within the

125 catalytic bed. Because of this, non-uniform temperature distributions were observed, as well as
126 stagnant and vortex flow regions, with both phenomena negatively affecting the performance of the
127 reactor [42]. Moreover, regions of low temperature posed a great risk for MeOH and H_2O
128 condensation [42]. In their subsequent work, they identified that condensation predominantly takes
129 place at the last 2 meters of the reactor and proposed different reactor configurations to prevent that
130 [41, 43]. Both Manenti *et al.* [56] and Rezaie *et al.* [47] simulated an industrial-scale MeOH synthesis
131 reactor using a 1D pseudo-homogeneous and a 1D pseudo-heterogeneous model. The pseudo-
132 homogeneous and the pseudo-heterogeneous models yielded similar and accurate results, both for
133 the steady-state and for the transient operation of the industrial reactor [47, 56], with the authors
134 suggesting the use of the pseudo-homogeneous model going forward, as it is both simpler to model
135 and faster to solve [56]. Manenti *et al.* [56] then used their model to perform a parametric study on
136 the industrial reactor, identifying the optimal operating temperature of the tube shell to be 526 K,
137 while also observing that carbon-rich feed compositions improve the MeOH yield but also increase
138 the hot-spot temperature [56]. Jamshidi *et al.* [40] performed a 2D CFD parametric investigation of
139 the MeOH synthesis reactor, where they estimated the MeOH yield resulting from changes in key
140 reactor parameters, such as the operating temperature and pressure, the flow rate, temperature, and
141 composition of the feed gas, and the reactor tube length and diameter. They identified that the flow
142 rate and composition were the most impactful parameters for MeOH synthesis and suggested an
143 optimised scenario which improved the MeOH yield compared to the baseline case [40]. However, the
144 impact of each of the aforementioned parameters was explored only for the MeOH yield, producing
145 a limited scope of the reactor operation.

146 By their nature, fixed bed chemical reactors involve multi-scale and multi-physics challenges, which
147 need to be accounted for. The structure and morphology of the catalytic bed affects both the
148 interparticle, e.g., velocity, pressure, and temperature, as well as the intraparticle, e.g., diffusion and
149 reaction, flow parameters. Studying each of these parameters in isolation results in a limited scope
150 and can neglect phenomena which are key for the reactor operation. Thus, a holistic investigation

151 approach is needed, which CFD models are uniquely positioned to offer. CFD models have been
152 instrumental in reaching a deeper understanding of fixed bed chemical reactors and their behaviour
153 [57-61]. Dixon identified that exothermic reactions produce a more homogeneous temperature
154 distribution within the bed, compared to endothermic reactions [62, 63]. Partopour and Dixon [64]
155 studied the fixed bed's reactor behaviour during the exothermic ethylene oxidation reaction, under
156 dynamic operation. They observed that, because of the different rates of interparticle convective
157 transfer and of intraparticle diffusion of oxygen, radial gradients in both the oxygen's concentration
158 and in the bed's temperature were observed [64]. This created a moving hot-spot, which increased in
159 magnitude as it traversed down the bed [64]. In our previous work, laboratory-scale fixed bed reactors,
160 formed by sieved catalytic particles, were scanned using computed-tomography (CT) and their internal
161 bed structure was analysed [65]. This shed light on the highly poly-dispersed nature of such fixed bed
162 systems, as a result of the complex forms and orientations of the catalytic particles [65]. A 3D
163 volumetric mesh was then generated from the CT-scanned images, allowing for CFD simulations [53,
164 66, 67]. The CFD simulations revealed a highly heterogeneous flow through the interparticle pores,
165 with the maximum velocity reached being 16-times higher than the average flow velocity [53].
166 Because of the holistic view generated from CFD models by coupling the bed structure with heat and
167 mass transfer phenomena, they are a valuable tool to utilise for reactor design optimisation.

168 While alternative reactor configurations have been examined for the Shiraz petrochemical reactor,
169 its overall design has mostly remained the same, i.e., consisting of 2962 tubes with each tube having
170 a length of 7.022 m and a diameter of 3.8 cm. Here, a single reactor tube is simulated using a 2D
171 pseudo-homogeneous CFD model, and its results are validated with the available experimental data.
172 Subsequently, an in-depth parametric study of the tube design is performed, with the length and the
173 diameter of the tube varying within the ±50% range from their baseline magnitudes, thus producing
174 53 cases in total. With the available data, a response surface was generated, revealing the
175 interconnection between the reactor design and the key operating parameters, i.e., the MeOH
176 production, the CO_2 and CO consumption, the flow velocity, and the temperature and pressure of the

177 catalytic bed. The generated response surface was then used for the goal-driven optimisation of the
178 reactor design by investigating two industrially relevant scenarios, leading to a higher, more economic,
179 and more environmentally friendly MeOH production.

180 Methodology

181 Experimental setup

182 The design and operating procedure of the industrial-scale MeOH synthesis reactor of Shiraz
183 petrochemical has been published [45, 47, 48], and is summarised in Table 1. In addition, detailed
184 information for the product composition at the outlet has also been published, thus allowing for model
185 validation.

Table 1: Design and operating procedure of the industrial-scale MeOH synthesis reactor of Shiraz petrochemical [45, 47, 48].

Reactor design		
Length	7.022	m
Diameter	$3.8e^{-2}$	m
Number of tubes	2962	-
Catalyst particle diameter	$5.4e^{-3}$	m
Catalyst density	1132	kg/m^3
Catalyst specific heat	50	J/(kg·K)
Catalyst particles thermal conductivity	4	W/(m·K)
Void fraction	0.39	-
Reactor operation		
CO_2	3.45	mol%
CO	4.66	mol%
H_2	79.55	mol%
H_2O	0.08	mol%
MeOH	0.03	mol%
CH_4	11.72	mol%
N_2	0.03	mol%
Feed flow rate	0.565	mol/s
Feed temperature	503	K
Operating pressure	76.98	bar
Operating temperature	523	K

Computational fluid dynamics model

Throughout this study, CFD simulations are performed with the ANSYS Fluent version 2022 R2 software. For the simulations, a 2D steady-state model is considered. Compared to a 3D model, the 2D model is not capable of reproducing the complex interconnectivity between the bed structure and the local flow field [62, 63], instead producing volumetrically-averaged flow profiles. However, it has the advantage of being considerably computationally cheaper than 3D models. With the goal of this study being design optimisation, a large number of cases should be examined, for which a fast and

accurate computational model is vital. Moreover, due to the size of industrial-scale fixed bed reactors, resolving the catalytic particles and thus accurately recreating the 3D bed structure, will quickly lead to unfeasible computational demands [61]. This restricts the modelling of industrial-scale reactors to either simpler 1D or 2D models or to changes in the modelling approach. Here, a 2D geometry with the porous medium model is used, which introduces the superficial velocity formulation, along with a sink in the momentum equation, S_i, to represent the pressure drop experienced by the flow due to the existence and morphology of the bed. The form of the mass, momentum, energy, and species conservation equations solved by Fluent [68, 69] are presented in eq. (1)-(4), respectively:

$$\nabla \cdot \left(\rho_f \vec{v}_f\right) = 0 \tag{1}$$

$$\nabla \cdot \left(\rho_f \vec{v}_f \vec{v}_f\right) = -\nabla P + \nabla \cdot \bar{\bar{\tau}} + \rho_f \vec{g} + S_i \tag{2}$$

$$\nabla \cdot \left(\vec{v}_f \left(\rho_f \frac{h_f}{M_{w,f}} + \rho_f \frac{{v_f}^2}{2}\right)\right) = \nabla \cdot \left(k_{eff} \nabla T_f - \sum_i \frac{h_{i,f}}{M_{w,i}} \vec{J_i} + \bar{\bar{\tau}}_f \cdot \vec{v_f}\right) + S_h \tag{3}$$

$$\nabla \cdot \left(\rho_f \vec{v}_f \varphi_i - \rho_f \mathfrak{D}_{eff,i} \nabla \varphi_i\right) = R_{i,j} \tag{4}$$

The momentum sink introduces a viscous and an inertial flow resistance term, which are determined by the Ergun [70] equation, shown in eq. (5)-(7). Here, ε_{inter} refers to the bed void fraction and is considered volumetrically constant for simplicity.

$$S_i = -\left(\frac{\mu_f}{\alpha} \vec{v}_f + C_{inert} \frac{1}{2} \rho_f \vec{v}_f \left|v_f\right|\right) \tag{5}$$

$$\frac{1}{\alpha} = \frac{150(1-\varepsilon_{inter})^2}{{d_p}^2 {\varepsilon_{inter}}^3} \tag{6}$$

$$C_{inert} = \frac{3.5(1-\varepsilon_{inter})}{d_p {\varepsilon_{inter}}^3} \tag{7}$$

The downside of Ergun's correlation for pressure drop is that its accuracy drops at high Reynolds flows, as the inertial term is not accurately resolved [71]. Alternative correlations have been proposed in the literature, such as Montillet *et al.* [72], Erdim *et al.* [73], and Dixon [74]. To evaluate Ergun's suitability for the case considered here, which has a Reynolds number of 220, comparative simulations were

performed with Ergun's and with Dixon's equations. The results are presented in Figure S3 of the ESI. Indeed, Ergun's equation overpredicts the pressure drop, but the difference between the two correlations is around 3%. This difference becomes much larger at flows with Reynolds numbers above 1000, and for such flows the use of Dixon's correlation is suggested [74]. In the literature, Nestler *et al.* [25], Rahimpour *et al.* [45], and Zahedi *et al.* [49], all simulate the same reactor using Ergun's correlation, while Rahmatmand *et al.* [46], and Mirvakili *et al.* [43], also use the Ergun's correlations with a slightly bigger reactor and with a faster reactant flow, i.e., 1.4 mol/s compared to 0.57 mol/s considered here. Hence, to keep consistent with literature data, and considering the small difference between the two correlations for low Reynolds number flows, Ergun's correlation was used here as well.

During the parametric study, an equation was needed to calculate the bed's void fraction, ε_{inter}, of the catalytic bed based on the design parameters of the reactor tube. Two semi-empirical correlations for the bed's void fraction were tested here, Achenbach's [75] and Dixon's [76]. For homogeneous spherical particles, Achenbach's correlation, eq. (8), predicts the void fraction to be equal to the experimental setup, i.e., 0.39, while Dixon's correlation predicts a void fraction of 0.41. This difference is reasonable, as Achenbach's correlation was derived to describe a close-packed bed while Dixon's correlation was derived to describe an open-packed bed. Considering that an industrial-scale reactor is modelled here, which is expected to follow a close-packed bed structure, Achenbach's correlation was used moving forward.

$$\varepsilon_{inter} = 0.78\left(\frac{d_p}{D_r}\right)^2 + 0.375 \tag{8}$$

Turbulence was accounted for using the k-ε model, denoted as $k_t - \varepsilon_t$, which introduces the following two equations [68]:

$$\frac{\partial}{\partial x_i}\left(\rho_f k_t u_{f,i}\right) = \frac{\partial}{\partial x_i}\left[\left(\mu_f + \frac{\mu_t}{\sigma_{k_t}}\right)\frac{\partial k_t}{\partial x_j}\right] + G_k - \rho_f \varepsilon_t - Y_M \tag{9}$$

$$\frac{\partial}{\partial x_i}\left(\rho_f \varepsilon_t u_{f,i}\right) = \frac{\partial}{\partial x_i}\left[\left(\mu_f + \frac{\mu_t}{\sigma_{\varepsilon_t}}\right)\frac{\partial \varepsilon_t}{\partial x_j}\right] + C_{1\varepsilon_t}\frac{\varepsilon_t}{k_t}G_k - C_{2\varepsilon_t}\rho_f \frac{{\varepsilon_t}^2}{k_t} \quad (10)$$

Where k_t is the turbulence kinetic energy, ε_t is the rate of dissipation, G_k is the generation of turbulence kinetic energy due to mean velocity gradients, Y_M is the contribution of the fluctuating dilatation in compressible turbulence to the overall dissipation rate, and $C_{1\varepsilon_t}$ and $C_{2\varepsilon_t}$ are constants with magnitudes of 1.44 and 1.92, respectively. Finally, σ_{k_t} and σ_{ε_t} are the Prandtl numbers for k_t and ε_t, respectively [68].

The standard k-ε model is applied here, with standard wall functions for near-wall treatment. The y^+ value in the baseline case is 2.5. Generally, the standard k-ε model less accurately resolves the near-wall region compared to alternative choices, such as the RNG k-ε model with enhanced wall treatment or the SST k-ω model [77, 78]. To evaluate the predictions of the standard k-ε model against those more advanced turbulence models, we ran simulations with the baseline case by utilising all three models. The results are presented in Figure S4 of the ESI, presented as axial profiles of MeOH mass fraction, pressure drop, temperature, and velocity magnitude. It can be seen that the standard k-ε model produces some deviations compared to the RNG k-ε and SST k-ω models, with the biggest error being observed in the MeOH mass fraction, equal to 7%, while the remaining three parameters have an error less than 1%. However, the RNG k-ε and SST k-ω models were comparatively more computationally expensive by 13% and 17%, respectively. The small error between the standard k-ε and the remaining two models in this work is primarily related to our approach of using a 2D case, which limits the radial complexity significantly. If instead a 3D case was used, then utilising a more accurate model would be key. With the goal of this work being the definition of a design space by simulating a large number of cases, we chose the standard k-ε model going forward as it produces reasonable predictions, coupled with more flexible meshing requirements and smaller simulation times.

Diffusion of species is applied volumetrically through the Dusty-Gas diffusion model [79] and details for the involved equations are presented in section 1.1. of the ESI. Similarly, chemical reactions are introduced volumetrically in each computational cell, following the form of eq. (11), as per ANSYS Fluent [68, 69]. To determine the reaction rate, the modified kinetic model from Nestler *et al.* [27] is applied here, as it was determined to be applicable for industrial-scale methanol production. The kinetic constants are all given in section 1.2 of the ESI.

$$R_{i,j} = \frac{\varepsilon_{bed}}{\tau_{bed}} \rho_{cat} \eta_j \sum_{j=1}^{N_R} v_{i,j} M_{w,i} r_{i,j} \tag{11}$$

$$r_{CO_2} = \frac{k_1 K_2 f_{CO_2} f_{H_2}^{1.5} \left(1 - \frac{f_{CH_3OH} f_{H_2O}}{f_{CO_2} f_{H_2}^3 K_{eq,1}}\right)}{\left(1 + K_1 f_{CO} + K_2 f_{CO_2}\right)\left(f_{H_2}^{0.5} + K_3 f_{H_2O}\right)} \tag{12}$$

$$r_{RWGS} = \frac{k_2 K_2 f_{CO_2} f_{H_2} \left(1 - \frac{f_{CO} f_{H_2O}}{f_{CO_2} f_{H_2} K_{eq,2}}\right)}{\left(1 + K_1 f_{CO} + K_2 f_{CO_2}\right)\left(f_{H_2}^{0.5} + K_3 f_{H_2O}\right)} \tag{13}$$

Applying the reactions volumetrically in each computational cell, however, unrealistically increases the active catalytic volume that would be otherwise available within the cell if the catalytic particles were resolved. This could be the reason why similar pseudo-homogeneous models predict faster reaction rates compared to particle-resolved CFD models where a realistic packed bed structure is generated [62, 63, 80]. Consequently, to approximate the local bed structure in each computational cell, the $\varepsilon_{bed}/\tau_{bed}$ factor is introduced, which is equal to the product of the interparticle structural factor, i.e., $\varepsilon_{inter}/\tau_{inter}$, and the intraparticle structural factor, i.e., $\varepsilon_{intra}/\tau_{intra}$. This results in a pseudo-homogeneous reaction rate term which only considers the available catalytic volume and local residence time instead of the full cell volume.

The term η_j in eq. (11), presented in more detail in section 1.2 of the ESI, represents the particle effectiveness factor, i.e., the fraction of reaction rate and of diffusion rate, used to dictate limitations to the overall reaction rate imposed by the rate of intraparticle diffusion of the reactants within the

catalytic particles [81]. Finally, the fugacity of species in eq. (12)-(13), f_i, is equal to the their local partial pressures multiplied by the fugacity coefficients calculated by the modified Soave-Redlich-Kwong equation [82].

Solution setup

The temperature of the tube wall was set to a constant magnitude of 523 K, while the operating pressure was set to 76.98 bar, following the operating procedure of the Shiraz petrochemical reactor. Although during the solution process the flow parameters were not tracked, a mesh independency study was conducted, presented in section 3.1 of the ESI, where the axial profiles of the key species and of temperature were examined for convergence. As will be discussed in the results section, the two finest meshes achieved excellent accuracy which builds confidence on model setup and solution convergence. The SIMPLE scheme for pressure-velocity coupling was introduced, with a 2nd-order upwind spatial discretization for each flow parameter. An under-relaxation factor of 0.3 was used for pressure and energy, of 0.5 for density, momentum, k_t, and ε_t, and of 0.7 for each chemical species. Residual targets were 5e^{-4} for all parameters except for energy, which was set to 1e^{-5}. Simulation proceeded until convergence was reached.

Goal-driven optimisation

A goal-driven optimisation is investigated in this paper, aiming to optimise the reactor design to best achieve two industrially relevant scenarios. For this, the tools available in the ANSYS DesignXplorer, version 2022 R2, are used. Parametric study and optimisation of the reactor are based on a three-step process, the initial definition of a design space, the generation of a response surface, and the use of the response surface to achieve the pre-set goals [83]. By determining a region of interest for the reactor design parameters (input parameters), sample points are generated thus defining a design space. Here, the design space is defined by shrinking and enlarging the reactor tube length and diameter within the 50% range from their baseline magnitudes, with the length dimension ranging in-between 3.5-10.5 m, and the diameter dimension ranging in-between 1.9-5.7 cm. For the length

dimension, 5 values were explored, while for the diameter dimension 9 values were explored. Priority is given to the tube's diameter, as it is more influential on heat and mass transfer phenomena compared to the tube's length.

In all these cases, the particle diameter was kept constant and equal to the baseline case, i.e., $5.4e^{-3}$ m. This simplifies both the integration of the flow resistances and of the particle effectiveness factor, whilst also allowing a systematic understanding of the impact of the reactor design. In fact, catalytic particles are very complex in nature and should be studied separately, as they have multiple aspects that can considerably affect chemical engineering applications, such as their sizes, shapes, orientations, and degradation [53, 54, 58, 65, 84-89]. A porous medium approach, such as the one utilised here for fast computations, is not suitable for this type of studies. The operating procedure, i.e., operating temperature and pressure, as well as inlet feed rate, composition, and temperature, remains constant and equal to the baseline case. In addition to the 45 cases outlined here, 8 additional cases were solved, with their length and diameter ranging in-between the design space created by the original 45 cases. These are used as refinement points for the response surface, allowing for a greater accuracy. The cases solved are all presented in Figure 1.

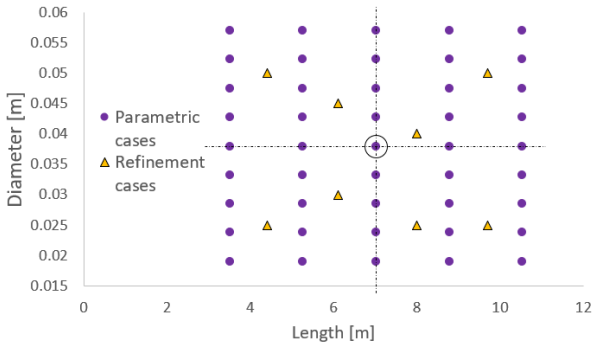

Figure 1: Parametric and refinement cases resulting from changes in the length and diameter dimensions of the reactor tube and used to generate the response surface. The circle in the middle represents the baseline reactor design, i.e., length of 7.022 m and diameter of 3.8 cm.

Following the solution of the 53 cases, the key parameters that define the operation of the reactor (output parameters) were collected. Specifically, these are: the MeOH, CO_2 and CO mass fractions at the outlet, the pressure drop, the flow velocity magnitude, the maximum temperature reached in the

reactor, and the catalyst mass. The minimum temperature could be another relevant parameter to look at from industrial perspective since dew point and MeOH/H_2O condensation is crucial for catalyst deactivation. The minimum temperature observed in our simulations was 229.5 ^oC, which is far above the dew point temperature of 125 ^oC reported by Keramat *et al.* [41]. As such, at this stage, dew point calculations were not introduced. However, expanding the reactor model by introducing condensation phenomena and investigating the impact of both design and operating parameters through a detailed parametric study can be considered for future work. With the available data, a response surface could then be generated which describes how changes in the input parameters affect the output parameters [83]. This allows response surfaces to approximate the values of output parameters within the design space without the need for additional simulations, acting as the cornerstone for goal-driven optimisations [83]. The response surface is generated through the genetic algorithm approach, and details for this method, as well as the metric used to assess its quality, are presented in section 2 of the ESI.

The generated and validated response surface is used to identify the reactor designs which best achieve the optimisation goals of the two considered scenarios. In the first scenario, the software is asked to maximise MeOH production while minimising the pressure drop of the reactor. In addition, the maximum reactor temperature should not exceed the upper safe operating temperature limit of the Cu/ZnO/Al_2O_3 catalyst, considered equal to 280 ^oC [25], which is lower than its sintering temperature reported to be 300 ^oC [39, 56]. In the second scenario, the same objectives are retained, but an additional goal was added, to also minimise the mass of catalyst used. Both scenarios attempt to maximise MeOH yield while reducing the operating and management costs, thus leading to both economic and environmental benefits. In both scenarios, the aforementioned goals hold equal importance, and a weight factor has not been introduced. This means that the optimisation software will not prioritise any goal and instead focus on identifying the candidates which best achieves all of them. The MOGA (Multi-Objective Genetic Algorithm) approach is used, which produces 400 population samples per iteration to fill the design space, select the best candidate points based on the

pre-set goals, and continue the iterations until the convergence criterion has been reached. The convergence criterion chosen is for 70% of the 400 sample points belonging to the pareto front.

Results and discussion

Prior to validating our CFD model and proceeding with the parametric and optimisation investigation, a mesh independency study was conducted. By gradually reducing the mesh element size, the dependency of the CFD results and of the flow parameters to the total mesh size can be evaluated, allowing the selection of the mesh size which achieves both accurate results and reduced computational costs. The results are presented in section 3.1 of the ESI. Out of the five different meshes considered, mesh independency is reached at the two finer meshes, with a total mesh size of 766k and 843k elements. These correspond to an element size of $6.6e^{-4}$ and $6.25e^{-4}$ m, respectively. The 766k mesh takes around 36 minutes to converge and has an average error of around 2.6% for the species mass fractions at the outlet. On the contrary, the 843k mesh takes around 43 minutes to converge, and has an average error of 2.3%. The $6.6e^{-4}$ m element size and 766k mesh were chosen for the computational study henceforth, given its minor difference in its computational error and faster computational time compared to the 843k mesh. To reduce the extend of this paper, only the key parameters are presented here, however all heat and mass transfer parameters are extensively examined and discussed. The reader can find all relevant results not present here in the extensive supplementary information document provided.

Model validation

Model validation is based on comparing the CFD model's predictions with available experimental data for the species composition, measured at the outlet. However, this provides limited knowledge of the species' behaviour within the catalytic bed. The non-inhibitive tracking of species is a big consideration for CFD model validation but also for kinetic model definition. Specifically, we highlighted in our previous work that two kinetic models for MeOH synthesis can produce almost identical species compositions in the outlet but can differ significantly in the predicted species behaviour and

interactions within the catalytic bed [26], hence leading to wrong assumptions for catalyst and reactor engineering. Potentially, a setup like the one used in Nestler *et al.* [27], where the temperature profile was also tracked along a demonstration-scale fixed bed reactor, could provide valuable additional information for CFD model validation. However, as such data is not available, our CFD model was validated using the outlet species composition from the experimental results of the Shiraz petrochemical reactor [45, 48], with the results presented in Figure 2. The CFD model reaches very accurate results for most of the species outlet mass fractions, with an error <1%, but presents some small deviations in the CO and H_2O mass fraction predictions, equal to -6.5% and 5.2%, respectively. These can be attributed to discrepancies in the reactions' equilibrium predictions from the KM, to imperfect operating control during the experimental procedure, or to simplifications in the CFD model. Regardless of its source, the overall absolute error of the CFD model is around 2.6%, which provides confidence for the model's accuracy moving forward.

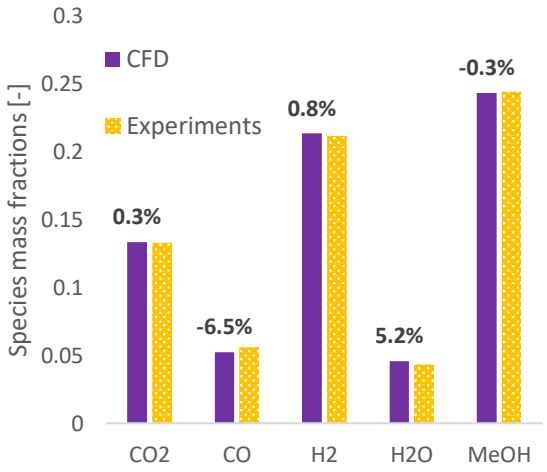

Figure 2: CFD model validation based on the outlet species composition of the Shiraz petrochemical reactor [45, 48].

The CFD results allow for a deeper investigation of the reactor's behaviour during operation, through the inspection of the key operating parameters. Specifically, the profiles of the species mass fractions, the pressure drop, and the temperature, integrated over 100 points along the entire axial length of the reactor, are presented in Figure 3. Respective profiles for the velocity magnitude and reaction rate are presented in Figure S5 of the ESI.

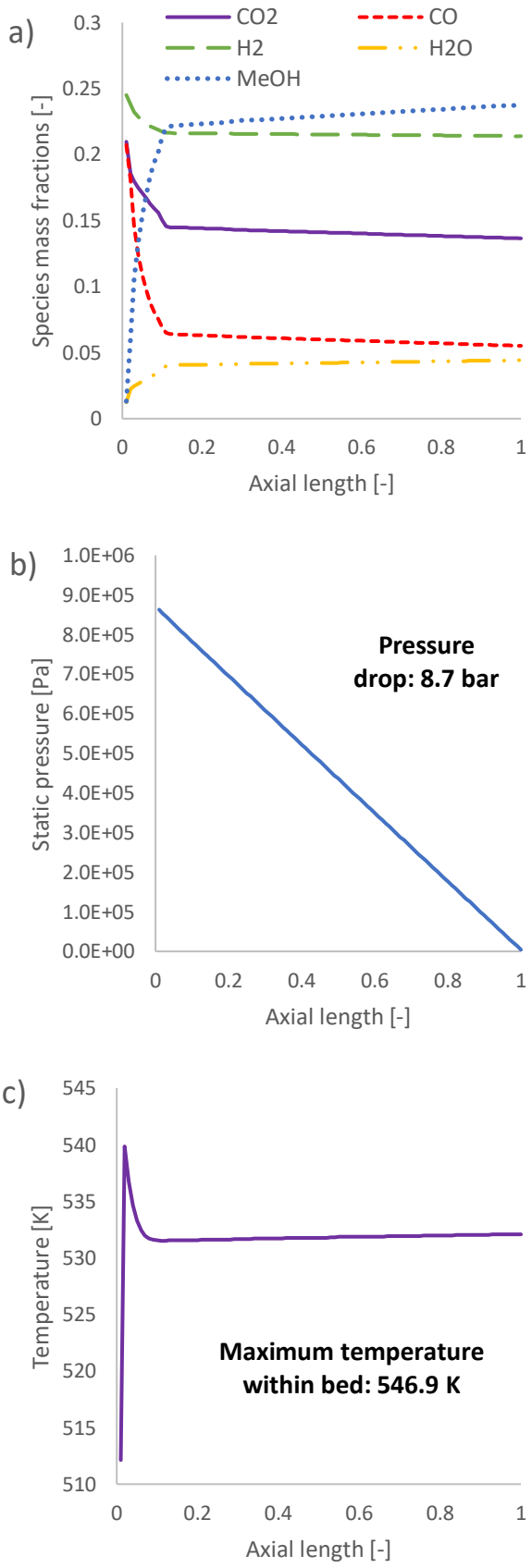

394 *Figure 3: Axially-integrated profiles of a) species mass fractions, b) pressure, and c) temperature of the baseline industrial-*
395 *scale MeOH reactor.*

396

The model predicts that the species reach chemical equilibrium early in the bed, around the axial length of 0.2, as per Figure 3a. Past that point, while reactions still occur up until the outlet of the reactor, as per Figure S5b of the ESI, their overall rate drops significantly. These are very similar profiles to those observed in our previous work for the laboratory-scale MeOH reactor [26] using the original KM of Nestler *et al.* [25]. The species profiles are attributed to the fast production of H_2O early in the bed due to the large magnitude of the CO_2 hydrogenation reaction, which pushes the species towards their equilibrium concentration and limits further chemical reactions [26]. This breaks the catalytic bed in two sections, the upper section where kinetics control the reaction rate, and the lower section where equilibrium controls the reaction rate, an observation reached by Rahimpour *et al.* [45] as well. Similar profile can be seen in the velocity magnitude, presented in Figure S5a of the ESI. Specifically, velocity magnitude drops until the axial length of around 0.2, where it plateaus. The large gradients in chemical species, flow density, and temperature in the top section of the bed cause the flow to decelerate, a process continuing until chemical equilibrium is achieved.

With both reactions proceeding towards their exothermic pathway, as per Figure S5b of the ESI, energy is released causing an increase in the temperature of the catalytic bed. This results in a temperature hot-spot in the region where the reaction rate magnitude is the highest, as can be seen in Figure 3c, which presents the integrated temperature at each axial location. The maximum temperature reached in the catalytic bed is 546.9 K, which is few degrees below the upper safe operating temperature limit for the $Cu/ZnO/Al_2O_3$ catalyst, i.e., 553 K. The CFD model predicts a pressure drop of 8.7 bar, which is around 11% of the operating pressure (Figure 3b). This is a considerable pressure drop, which could significantly increase the compressor power requirements, thus reducing the overall efficiency of the system and increasing the operating costs. Moreover, excessive pressure drops are associated with lower reaction rates [46], as the fugacity of the species, and hence the driving force of the reaction, are reduced along the catalytic bed.

By comparing the temperature profile predicted from the CFD model with respective profiles produced from computational models of other researchers, we can further testify the validity of our model. The 1D models of Kordabadi and Jahanmiri [50], Rezaie *et al.* [47], and Nestler *et al.* [25], all simulate the same reactor but with different feed compositions, hence the temperature magnitude will differ. However, while the 1D models also predict a temperature hot-spot early in the bed, their predicted temperature profiles follow a much smoother and gradual upward and downward trend compared to what is seen here. On the CFD model of Jamshidi *et al.* [40] a bigger reactor is investigated, with a reactor length of 9 m and a tube diameter of 5.75 cm. However, their temperature profile follows the characteristic slope seen here, i.e., a fast temperature increase near the reactor entrance reaching a single peak, followed by a smooth temperature drop [40]. Compared to our model, a plateau is not reached in Jamshidi *et al.* [40], which can be attributed to them studying both a different reactor configuration and operating procedure. Consequently, the 1D mathematical models and the 2D CFD models do not predict the same temperature profiles. The temperature profile is the result of various terms, as per the energy conservation equation, eq. (314), which involves convection, diffusion, conduction, and reaction. The 1D models of Kordabadi and Jahanmiri [50], Rezaie *et al.* [47], and Nestler *et al.* [25] only solve for conduction, reaction, and heat exchange between solid and fluid phase, i.e., pseudo-heterogeneous approach, thus do not solve for convection and diffusion. This is contrary to the CFD models, which solve for all 4 terms. As discussed in our previous work, convection is a considerable energy term which should be accounted for [61]. Its primary term is velocity, whose magnitude is the highest near the reactor entrance and parabolically plateaus at an axial length of 0.1, as per Figure S5a of the ESI. The combination of fast chemical reactions in the reactor entrance, coupled with the convection profile dictated by velocity, produces the temperature profile seen here and in the study of Jamshidi *et al.* [40]. The agreement of our CFD model both with the experimental data and with literature trends builds confidence in the computational predictions, paving the way for the parametric study presented in the next section.

Response surface investigation

The quality of fit of the produced response surface is presented in Figure S6 of the ESI, where the CFD-produced data occupy the X-axis and the response surface-predicted data occupy the Y-axis. The response surface achieves excellent accuracy for the examined flow parameters, with its predictions being almost identical to the CFD model results. Consequently, the various data points of Figure S6 are located on top of the X=Y centreline. The excellent accuracy of the response surface is also verified by the three quality metrics, i.e., coefficient of determination, root mean square error, and relative average absolute error, with the results presented in Table S3 of the ESI. All three metrics, and for both data point and cross-validation assessments, are close to their ideal values, with the biggest deviation, equal to 5.7%, being in the cross-validation of the temperature profiles.

The 3D response surface and 2D axis plots of MeOH mass fraction, pressure drop, and maximum temperature reached in the reactor, as a function of the length and the diameter of the reactor's tube, are presented in Figure 4. The 2D plots present the change of the output parameters as a function of one of the input parameters, while the secondary parameter is set to its baseline value, i.e., 7.022 m for the length dimension and $3.8e^{-2}$ m for the diameter dimension. Respective plots for CO_2 and CO mass fractions, as well as for velocity magnitude, are presented in Figure S7 of the ESI. The 3D graphs are also provided for the reader to interact with and inspect deeper in ".oggu" format, produced by the Origin 2022b software.

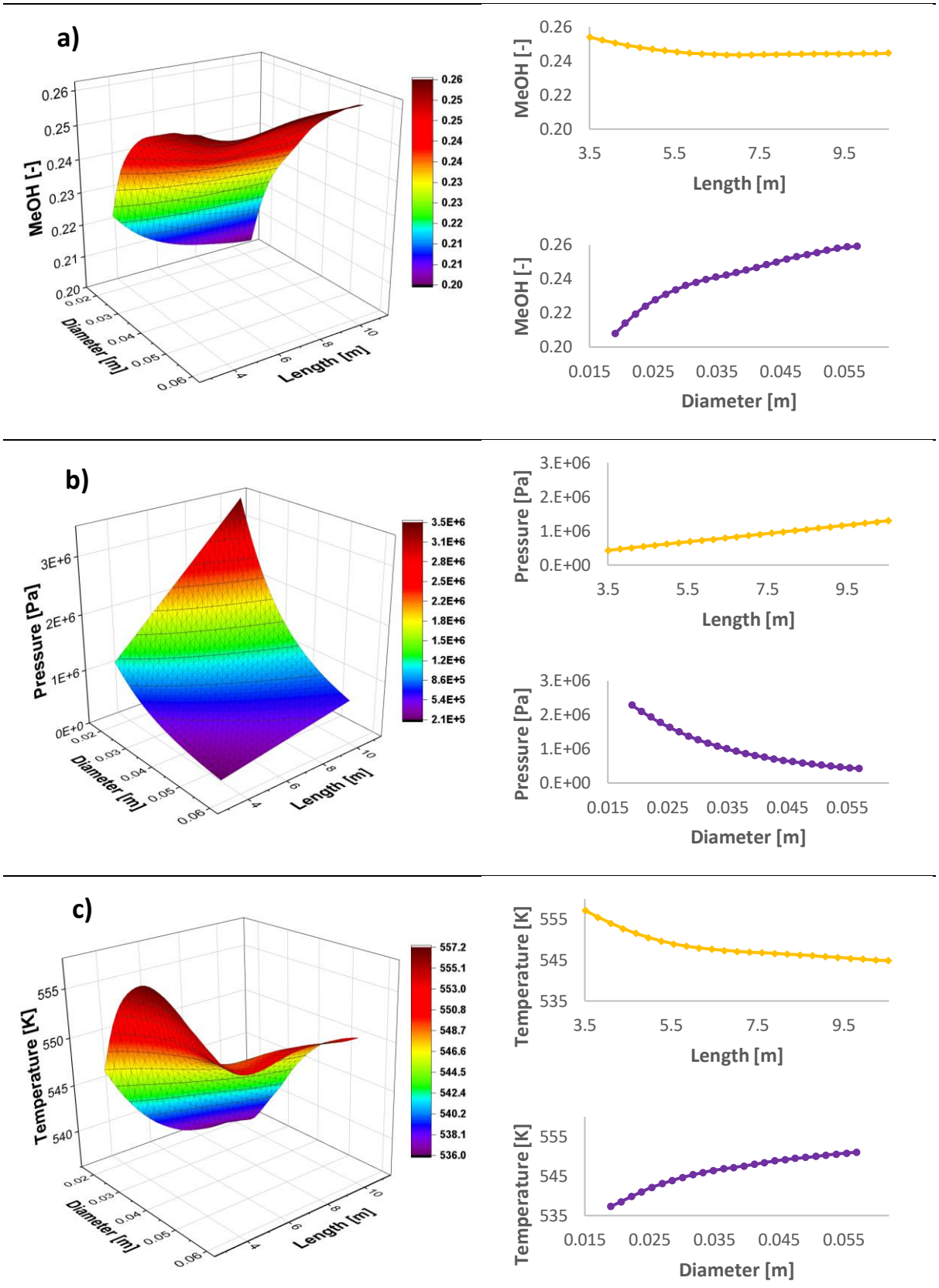

Figure 4: 3D response surface and 2D axis plots of a) MeOH mass fraction, b) pressure drop, and c) maximum temperature, as a function of the reactor tube's length and diameter dimensions.

As per Figure 4, MeOH production is negatively affected by the increase of the reactor's length and positively affected by the increase of the reactor's diameter. MeOH is less sensitive to changes in the reactor's length compared to its diameter, decreasing by around 1% as length increases from 3.5 m to 10.5 m and increasing by 5% as diameter increases from 1.9 cm to 5.7 cm. To understand this behaviour, the remaining parameters must be examined.

Pressure drop is positively affected by the increase of the reactor's length and negatively affected by the increase of the reactor's diameter. Surprisingly, pressure is less sensitive to the reactor's length than its diameter. As the reactor's length increases, pressure increases by 8.7 bar, while as the reactor's diameter increases, pressure reduces by 18.6 bar. The reactor's length has a marginal impact in the flow velocity (Figure S7c, ESI), thus, as per the momentum equation, eq. (2), it solely impacts the pressure drop through the ∇P term. On the contrary, the reactor's diameter has a double impact on the reactor's pressure drop. As the diameter increases, the bed's void fraction, ε_{inter}, eq. (8), is reduced. By keeping the particle diameter, d_p, constant, this translates into increased flow resistances, dictated by the Ergun equations, eq. (5)-(7), and thus a higher pressure drop at higher reactor diameters. However, because it was decided to keep the feed flow rate constant throughout, the increase of the tube's diameter translates into a considerable reduction in the flow velocity. Specifically, velocity drops from 22.8 m/s at a reactor diameter of 1.9 cm to 7.4 m/s at a reactor diameter of 5.7 cm, as per Figure S7c of the ESI. On the contrary, the reactor's length has a comparatively marginal influence over the flow's velocity magnitude, as per Figure S7c of the ESI. With velocity having a 1st-order and 2nd-order correlation with the viscous and inertial resistances, as per eq. (5), its effect takes precedent over the increased flow resistances, and a lower pressure drop at higher reactor diameters is observed. Consequently, due to the lower pressure drop imposed by shorter tube lengths and larger tube diameters, the local fugacity and partial pressure of the individual species is positively affected, increasing the overall reaction rate and MeOH production compared to smaller tube diameters.

The bed's maximum temperature is negatively affected by the increase in the reactor's length and positively affected by the increase of the reactor's diameter. However, temperature is almost equally sensitive to both dimensions, presenting changes of around 12.2 K and 13.7 K for length and diameter, respectively. As mentioned in the introduction, fixed-bed chemical reactors are cooled by water or gas flowing through the outer tube wall. Consequently, the reactor's length should not affect the heat removal process significantly, as it simply increases the outer surface area that the coolant needs to flow through. However, expanding the reactor's diameter reduces the heat removal rate [57], especially in the central bed regions, thus increasing the risk for extreme local hot-spots and run-away conditions. These conclusions are evident in Figure 4. Smaller reactor lengths result in higher temperatures primarily because of the higher reaction rates observed. As discussed, shorter tube lengths and wider tube diameters decrease the pressure drop, hence positively affecting the species' fugacity and the reactions' driving force. Consequently, due to the faster reaction rates, the exothermic energy released is enhanced and the local temperature is increased, as seen in Figure 4a. On the contrary, smaller tube diameters make heat removal easier, hence why the catalytic bed reaches smaller maximum temperatures, as per Figure 4c, resulting in considerably lower MeOH production as well.

The CO_2 and CO mass fractions, Figures S7a and S7b of the ESI, respectively, present a very similar response to changes in the tube design. Discussion here is focused on CO_2 and CO consumption, rather than on CO_2 and CO mass fractions. CO_2 and CO consumption is negatively affected by the increase in the reactor's length and positively affected by the increase in the tube's diameter, i.e., the outlet CO_2 and CO mass fractions are reduced at lower length and higher diameter dimensions. The same reasons that benefit or hinder MeOH production are also affecting CO_2 and CO consumptions, as the three species are directly related through their chemical pathways.

The analysis of the produced response surface reinforces the need to examine the reactor holistically, as all parameters are interconnected and directly influenced by the reactor design. For example,

516 increasing the reactor's diameter and only observing the species behaviour would neglect its
517 considerable influence on pressure drop, velocity, and temperature. Validated CFD models are crucial
518 for such holistic investigations and can pave the way for next-generation catalyst and reactor
519 engineering.

520 ## Goal-driven optimisation – Scenario 1

521 The optimisation software produced 4000 sample points, presented in Figure S8 of the ESI over 9
522 iterations. Based on these samples, local optimisation then identified the pareto front, presented in
523 Figures S9 and S10 of the ESI. MeOH mass fraction decreases at higher pressure drops (Figure S10a,
524 ESI) and increases at higher reactor temperatures (Figure S10b, ESI). Moreover, temperature
525 decreases at higher pressure drops (Figure S10c, ESI). For this scenario, the optimisation algorithm
526 predicts the pareto front to exist in higher reactor diameters and smaller reactor lengths, as per Figure
527 S9 of the ESI, allowing for higher overall MeOH production and lower pressure drops, whilst avoiding
528 exceeding the pre-set temperature limit. From these results, the software identifies the three best
529 reactor candidates, presented in Table S4 of the ESI, which also showcases the key operating
530 parameters as predicted by the response surface. The performance differences between the three
531 candidates are marginal, and all three of them perform better than the baseline reactor. The first
532 candidate was selected here to produce a 2D geometry from and simulate with the CFD software.
533 Specifically, the chosen reactor has a length of 3.6 m and a diameter of 5.67 cm. The MeOH mass
534 fraction, pressure drop, and temperature axial profiles of the optimised reactor are presented in
535 Figure 5, while the remaining parameters, i.e., species mass fractions, reaction rate, and velocity
536 magnitude, are presented in Figure S11 of the ESI. As a comparison, the profiles from the baseline
537 reactor, i.e., with a length of 7.02 m and a diameter of 3.8 cm, are also presented.

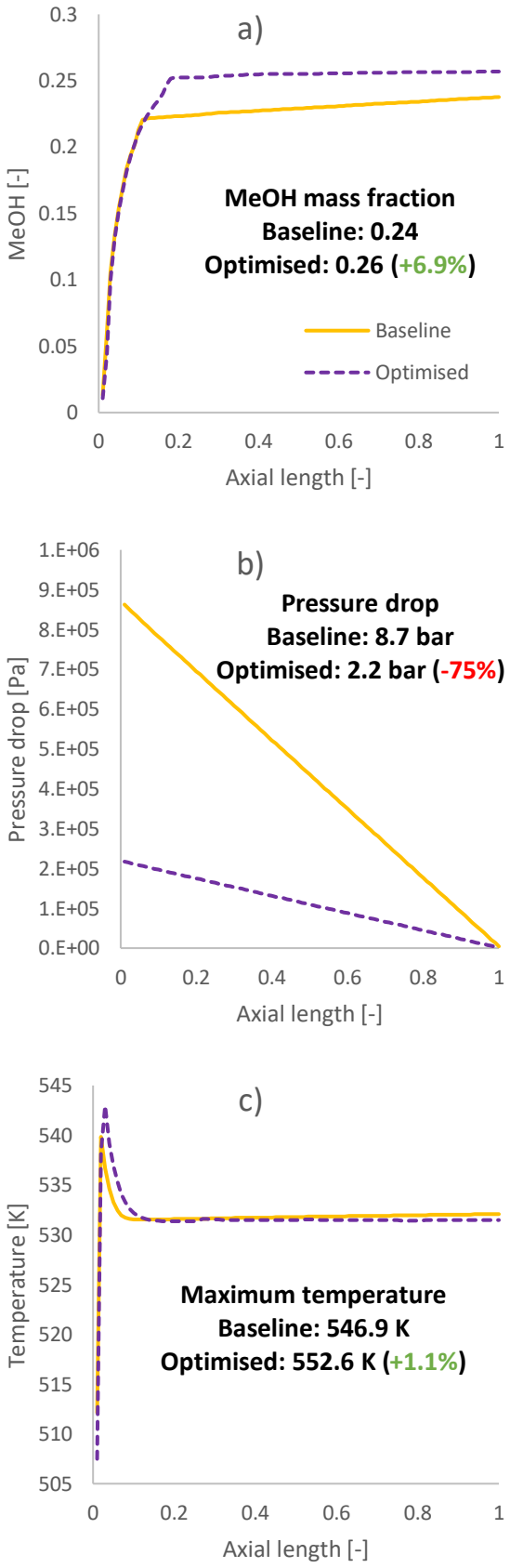

538 *Figure 5: Baseline and optimised reactor a) MeOH mass fraction, b) pressure drop, and c) maximum temperature axial*
539 *profiles, for optimisation scenario 1.*

The optimised reactor achieves 6.9% higher MeOH production, while its pressure drop is reduced significantly by 75%. In addition, the CO_2 and CO consumption, compared to the baseline, is increased by 6.7% and 19.5%, respectively. For the optimised reactor, reactions reach equilibrium deeper into the bed, as per Figure S11b of the ESI, thus the kinetically controlled section of the bed is expanded, allowing for MeOH to reach higher concentrations. Past the equilibrium depth, however, the reaction rate magnitude of the optimised reactor is lower than that of the baseline reactor. This explains why a plateau is reached for MeOH in the optimised reactor, while MeOH production continues past the equilibrium depth for the baseline reactor (Figure 5a). With the exothermic reactions being the primary drivers of the bed's temperature, the hot-spot now penetrates deeper into the bed and reaches a higher magnitude for the optimised reactor, as per Figure 5c, with the maximum temperature reached being 1.1% higher than the baseline reactor. However, the upper temperature constraint of 280 ^{o}C is not exceeded. Given its morphology, the optimised reactor has a 11.5% higher catalyst load compared to the optimised reactor.

Overall, the optimised reactor of scenario 1 achieves its goals of higher MeOH production, by 6.9%, and a reduced pressure drop, by 75%. Moreover, it achieves a considerably higher CO_2 and CO consumptions per reactant pass compared to the baseline case. These results can all benefit the techno-economic feasibility of the MeOH synthesis plant, as the compressor energy requirements are considerably reduced while the revenues from MeOH and CO_2-credits can be increased. The increase in the temperature profile and in the catalyst mass could increase the OpEx, but with them not being the marginal cost-drivers, their contribution should be small.

Goal-driven optimisation - Scenario 2

The optimisation software produced 2500 sample points, presented in Figure S12 of the ESI, over 7 iterations. By focusing on smaller tube lengths and intermediate tube diameters (Figure S13, ESI), local optimisation identified the pareto front seen in Figure S14 of the ESI. For this scenario, MeOH mass fraction increases with the increase in the catalyst mass (Figure S14c, ESI), while both MeOH mass

565 fraction and catalyst mass are reduced with the increase of the pressure drop, as per Figure S14a and
566 S14d of the ESI, respectively. Instead, temperature presents a more random spread of values with the
567 remaining three parameters. The three candidates identified by the software are presented in Table
568 S5 (ESI), and further CFD simulation results are presented here for the first candidate which achieved
569 the highest reduction in the catalyst mass. In this case, the reactor tube has a length of 4.1 m and a
570 diameter of 3.25 cm. The MeOH mass fraction, pressure, and temperature axial profiles are presented
571 in Figure 6, while the axial profiles of the remaining species mass fractions, the reaction rate
572 magnitudes, and the velocity magnitude are presented in Figure S15 of the ESI.

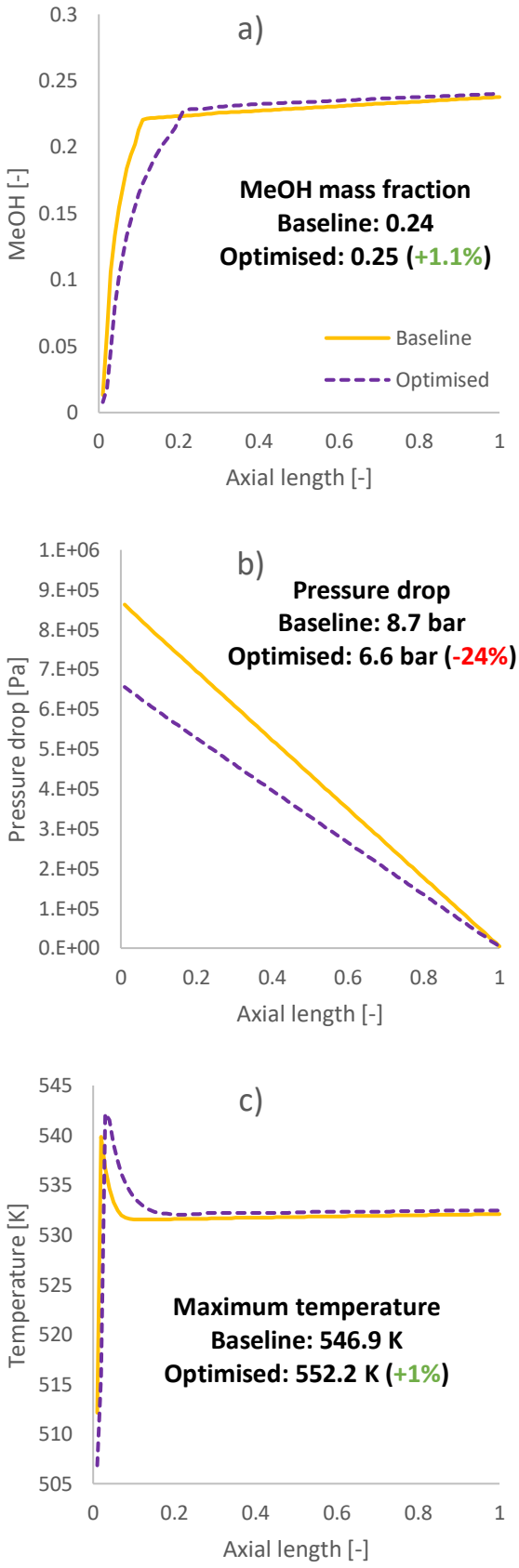

573 *Figure 6: Baseline and optimised reactor a) MeOH mass fraction, b) pressure drop, and c) maximum temperature axial*
574 *profiles, for optimisation scenario 2.*

Compared to the baseline reactor, the optimised reactor in this scenario achieves a 1.1% increase in MeOH production with a 56.5% decrease in the catalytic load. Simultaneously, CO_2 and CO consumptions are increased by 1.2% and 1.9%, respectively, whilst the pressure drop is reduced by 24%. Instead of reaching equilibrium early on, reactions are slower in this scenario and penetrate deeper into the catalytic bed, as per Figure S15b (ESI), as a result of the faster velocity profile in this case (Figure S15c, ESI). Consequently, MeOH production is slow near the entrance but eventually exceeds the baseline reactor's production around the axial depth of 0.2 (Figure 6a). Past this length, the reactions of the optimised reactor also reach equilibrium. Following the exothermic reaction rates' profile, the temperature profile of the optimised reactor is lower than that of the baseline reactor near the entrance. However, as the reaction rates magnitudes of the optimised reactor exceed those of the baseline reactor deeper into the bed, the optimised reactor reaches a 1% higher hot-spot magnitude but remains below the temperature constraint of 280 ^{o}C (Figure 6c).

The optimised reactor for this scenario also achieves all its pre-set goals, allowing for more MeOH production, less catalytic material, and smaller pressure drops. However, this scenario might not be as economically sensible as the first scenario. The first scenario achieves a comparatively higher MeOH production and a considerably lower pressure drop, despite having 11.5% more catalytic load. The techno-economical analyses suggest [15, 28-31] that prioritising the increase of the MeOH yield and the reduction of the pressure drop is expected to have a bigger economic and environmental impact compared to reducing the catalyst load, given the marginal cost of the catalyst. However, the long-term availability of Cu and Zn could potentially change this dynamic [90].

Here, all the pre-set goals were assigned equal importance. However, further optimisation of the industrial MeOH reactor could be aided through industrial involvement. This will allow for weight factors to be introduced in the different pre-set goals, allowing the software to identify what goals to prioritise. Moreover, new goals could also be added. A consideration that was not taken into consideration in this study is land area limitations to the reactor assembly design. The full MeOH-

synthesis reactor consists of 2962 tubes, thus changing the dimensions of a single tube will considerably change the dimensions of the system, and potentially of the overall plant. Combining our CFD model with a plant feasibility study, which can set predetermined area availability, operating constraints, and production goals, could accelerate the adoption of carbon-neutral MeOH synthesis applications, whilst improving the cost competitiveness of MeOH. The coupling of system-level models, such as Aspen, which focus on optimising the plant operation, with sub-system-level models, such as CFD, which focus on optimising individual components, i.e., the MeOH reactor or the H_2O electrolysis system, could yield crucial data to improve our chemical industries and achieve our climate goals. Beyond MeOH synthesis, however, the proposed validated CFD model can be a valuable tool for any chemical process, helping to advance the technology readiness level and accelerate commercialisation. The flexibility of CFD models to be applied both for fundamental research, i.e., investigate the kinetics of reactions, and for large-scale engineering projects, as was done here, positions them in the forefront to tackle the next-generation engineering challenges.

Conclusions

The wide availability of carbon-neutral methanol is key to reduce the dependence of maritime transportation on fossil fuels and reduce its greenhouse gas emissions. Methanol can be synthesized from CO_2, CO, and H_2 in heterogeneous fixed bed chemical reactors. However, to accelerate the bulk production of MeOH whilst improving its cost competitiveness, fixed bed chemical reactors need to be well-understood and optimised. For this purpose, Computational Fluid Dynamics (CFD) models can play a vital role. Here, a 2D CFD model is developed to simulate a single tube out of a multi-tubular industrial-scale MeOH-synthesis reactor, following the operating procedure published in the literature. The CFD results were validated based on available experimental data, yielding excellent accuracy. The model predicts that reactions are rapid near the bed entrance and reach equilibrium at an axial depth of 0.2. Due to reaction exothermicity, a temperature hot-spot is generated, with the

maximum temperature reached being equal to 546.9 K. Moreover, a considerable pressure drop of 8.7 bar is predicted, which can increase the compressor demands.

A detailed parametric study was performed to better understand the reactor's behaviour. The results allowed for the generation of a response surface, which revealed the sensitivity of MeOH production, pressure drop, and maximum reactor temperature to the reactor tube's design. Using these results, a goal-driven optimisation was conducted, investigating two industrially-relevant scenarios to maximise MeOH yield whilst minimising the pressure drop and preventing the reactor's temperature to exceed the safe temperature limit for the $Cu/ZnO/Al_2O_3$ catalyst. The optimised reactor design achieved a 6.9% increase in MeOH production and a 75% reduction in the pressure drop compared to the baseline reactor, thus paving the way for more economic and sustainable MeOH synthesis.

Acknowledgements

The authors would like to thank the Industrial Decarbonisation Research and Innovation Centre (IDRIC), grant number EP/V027050/1, for their funding.

Nomenclature

Symbols	Meaning	Units
C_{inert}	Inertial resistance	$[m^{-1}]$
$\mathcal{D}_{eff,i}$	Effective diffusivity (determined through the dusty gas model)	$[m^2/s]$
$\mathcal{D}_{ij_{eff}}$	Binary diffusion coefficient between species "i" and "j"	$[m^2/s]$
$D_{i,m}$	Bulk diffusivity of species "i" in mixture "m"	$[m^2/s]$
$D_{kn,i}$	Knudsen diffusion coefficient of species "i"	$[m^2/s]$
D_r	Reactor tube diameter	$[m]$
d_p	Particle diameter	$[m]$
d_{pore}	Pore diameter	$[m]$
f_i	Fugacity of species "i"	$[bar]$
$\vec{g}$	Gravitational acceleration	$[m/s^2]$
h_f	Enthalpy of fluid phase	$[J/kmol]$
$\vec{J_i}$	Diffusion flux	$[kg/(m^2 s)]$

$K_{eq,j}$	Equilibrium constant of reaction "j"	$[variable\ units]$
K_i	Adsorption coefficient of species "i"	bar^{-1}
k_{eff}	Effective thermal conductivity of porous medium	$[W/(mK)]$
k_j	Kinetic constant of reaction "j"	$kmol/(m_{cat}^3 \cdot sec \cdot bar^{1.5})$
k_t	Turbulent kinetic energy	$[m^2/s^2]$
$M_{w,f}$	Molar mass of fluid phase	$[kg/kmol]$
N_i	Molar flux of species "i"	$[kmol/(m^2 s)]$
P	Static pressure	$[Pa]$
$R_{i,j}$	Reaction source for species "i" along reaction pathway "j"	$[kg/(m^3 s)]$
S_h	Enthalpy source	$[W/m^3]$
S_i	Momentum source	$[Pa/m]$
T_f	Temperature of fluid phase	$[K]$
$\vec{v}_f$	Velocity of fluid phase	$[m/s]$
v_i	Atomic diffusion volume	[-]
$v_{i,j}$	Stoichiometric coefficient of species "i" in reaction "j"	[-]
X_i	Mol fraction of species "i"	[-]
Greek Symbols	**Meaning**	**Units**
α	Viscous resistance	$[m^2]$
ΔH	Enthalpy change	$[kJ/mol]$
ε_{bed}	Total bed porosity (intraparticle and interparticle)	[-]
ε_{inter}	Interparticle porosity, i.e., bed void fraction	[-]
ε_{Intra}	Intraparticle porosity	[-]
ε_t	Ratio of dissipation	$[m^2/s^3]$
η_j	Effectiveness factor for reaction "j"	[-]
μ_f	Viscosity of fluid phase	$[kg/(m\ s)]$
μ_t	Turbulent viscosity of fluid	$[kg/(m\ s)]$
ρ_{cat}	Density of catalyst	$[kg/m^3]$
ρ_f	Density of fluid phase	$[kg/m^3]$
σ_i	Prandtl number	[-]
$\bar{\bar{\tau}}$	Stress tensor	$[Pa]$
τ_{bed}	Total bed porosity (intraparticle and interparticle)	[-]
τ_{Intra}	Intraparticle tortuosity	[-]
φ_i	Scalar quantity "i" (represents species mass fractions)	[-]
φ_j	Thiele modulus	[-]
Abbreviations	**Meaning**	**Units**
CaPex	Capital Expenses	[-]
CFD	Computational Fluid Dynamics	[-]
OpEx	Operating Expenses	[-]

638

References

[1] R. Grynspan, "Review of Maritime Transport 2022," *United Nations Conference on Trade and Development,* 2022.

[2] Directorate-General for Climate Action. "Reducing emissions from the shipping sector." European Commission,. https://climate.ec.europa.eu/eu-action/transport/reducing-emissions-shipping-sector_en (accessed 2023).

[3] Elizabeth Connelly, Jacob Teter, and L. Cret. "International Shipping." International Energy Agency (IEA). https://www.iea.org/energy-system/transport/international-shipping (accessed.

[4] G. Hutchings *et al.*, *Sustainable synthetic carbon based fuels for transport, Policy Briefing*. London: The Royal Society, 2019/9/20.

[5] IPCC. "Global Warming of 1.5 °C, An IPCC Special Report on the impacts of global warming of 1.5 °C above pre-industrial levels and related global greenhouse gas emission pathways, in the context of strengthening the global response to the threat of climate change, sustainable development, and efforts to eradicate poverty." World Meteorological Organization, Geneva, Switzerland. https://www.ipcc.ch/sr15/chapter/spm/ (accessed.

[6] C. Kouridis and C. Vlachokostas, "Towards decarbonizing road transport: Environmental and social benefit of vehicle fleet electrification in urban areas of Greece," *Renewable and Sustainable Energy Reviews,* vol. 153, p. 111775, 2022/01/01/ 2022, doi: https://doi.org/10.1016/j.rser.2021.111775.

[7] W. Ke, S. Zhang, Y. Wu, B. Zhao, S. Wang, and J. Hao, "Assessing the Future Vehicle Fleet Electrification: The Impacts on Regional and Urban Air Quality," *Environmental Science & Technology,* vol. 51, no. 2, pp. 1007-1016, 2017/01/17 2017, doi: 10.1021/acs.est.6b04253.

[8] W. J. Smith, "Can EV (electric vehicles) address Ireland's CO2 emissions from transport?," *Energy,* vol. 35, no. 12, pp. 4514-4521, 2010/12/01/ 2010, doi: https://doi.org/10.1016/j.energy.2010.07.029.

[9] A. Soret, M. Guevara, and J. M. Baldasano, "The potential impacts of electric vehicles on air quality in the urban areas of Barcelona and Madrid (Spain)," *Atmospheric Environment,* vol. 99, pp. 51-63, 2014/12/01/ 2014, doi: https://doi.org/10.1016/j.atmosenv.2014.09.048.

[10] G. A. Olah, T. Mathew, A. Goeppert, and G. K. Surya Prakash, "Difference and Significance of Regenerative Versus Renewable Carbon Fuels and Products," *Topics in Catalysis,* vol. 61, no. 7, pp. 522-529, 2018/06/01 2018, doi: 10.1007/s11244-018-0964-8.

[11] The Solent Cluster. "Working together for a lower carbon future." https://www.thesolentcluster.com/ (accessed.

[12] G. Bozzano and F. Manenti, "Efficient methanol synthesis: Perspectives, technologies and optimization strategies," *Progress in Energy and Combustion Science,* vol. 56, pp. 71-105, 2016/09/01/ 2016, doi: https://doi.org/10.1016/j.pecs.2016.06.001.

[13] F. Dalena, A. Senatore, A. Marino, A. Gordano, M. Basile, and A. Basile, "Chapter 1 - Methanol Production and Applications: An Overview," in *Methanol*, A. Basile and F. Dalena Eds.: Elsevier, 2018, pp. 3-28.

[14] G. A. Olah, "Towards Oil Independence Through Renewable Methanol Chemistry," *Angewandte Chemie International Edition,* vol. 52, no. 1, pp. 104-107, 2013, doi: 10.1002/anie.201204995.

[15] J. Nyári, M. Magdeldin, M. Larmi, M. Järvinen, and A. Santasalo-Aarnio, "Techno-economic barriers of an industrial-scale methanol CCU-plant," *Journal of CO2 Utilization,* vol. 39, p. 101166, 2020/07/01/ 2020, doi: https://doi.org/10.1016/j.jcou.2020.101166.

[16] H.-J. Wernicke, L. Plass, and F. Schmidt, "Methanol Generation," in *Methanol: The Basic Chemical and Energy Feedstock of the Future: Asinger's Vision Today*, M. Bertau, H. Offermanns, L. Plass, F. Schmidt, and H.-J. Wernicke Eds. Berlin, Heidelberg: Springer Berlin Heidelberg, 2014, pp. 51-301.
[17] J. M. Thomas and W. J. Thomas, *Principles and practice of heterogeneous catalysis*, Second, revised edition. ed. Wiley-VCH, 2015.
[18] E. J. S. G.H. Graaf, A.A.C.M. Beenackers, "Kinetics of low-pressure methanol synthesis," *Chemical Engineering Science,* vol. 43, no. 12, pp. 3185-3195, 1988, doi: 10.1016/0009-2509(88)85127-3.
[19] G. H. Graaf, H. Scholtens, E. J. Stamhuis, and A. A. C. M. Beenackers, "Intra-particle diffusion limitations in low-pressure methanol synthesis," *Chemical Engineering Science,* vol. 45, no. 4, pp. 773-783, 1990/01/01/ 1990, doi: https://doi.org/10.1016/0009-2509(90)85001-T.
[20] N. Park, M.-J. Park, Y.-J. Lee, K.-S. Ha, and K.-W. Jun, "Kinetic modeling of methanol synthesis over commercial catalysts based on three-site adsorption," *Fuel Processing Technology,* vol. 125, pp. 139-147, 2014/09/01/ 2014, doi: https://doi.org/10.1016/j.fuproc.2014.03.041.
[21] G. Liu, D. Willcox, M. Garland, and H. H. Kung, "The role of CO2 in methanol synthesis on Cu・Zn oxide: An isotope labeling study," *Journal of Catalysis,* vol. 96, no. 1, pp. 251-260, 1985/11/01/ 1985, doi: https://doi.org/10.1016/0021-9517(85)90378-1.
[22] G. C. Chinchen, P. J. Denny, D. G. Parker, M. S. Spencer, and D. A. Whan, "Mechanism of methanol synthesis from CO2/CO/H2 mixtures over copper/zinc oxide/alumina catalysts: use of14C-labelled reactants," *Applied Catalysis,* vol. 30, no. 2, pp. 333-338, 1987/04/15/ 1987, doi: https://doi.org/10.1016/S0166-9834(00)84123-8.
[23] M. Saito, T. Fujitani, M. Takeuchi, and T. Watanabe, "Development of copper/zinc oxide-based multicomponent catalysts for methanol synthesis from carbon dioxide and hydrogen," *Applied Catalysis A: General,* vol. 138, no. 2, pp. 311-318, 1996, doi: 10.1016/0926-860x(95)00305-3.
[24] K. M. V. Bussche and G. F. Froment, "A Steady-State Kinetic Model for Methanol Synthesis and the Water Gas Shift Reaction on a Commercial Cu/ZnO/Al2O3Catalyst," *Journal of Catalysis,* vol. 161, no. 1, pp. 1-10, 1996/06/01/ 1996, doi: https://doi.org/10.1006/jcat.1996.0156.
[25] F. Nestler *et al.*, "Kinetic modelling of methanol synthesis over commercial catalysts: A critical assessment," *Chemical Engineering Journal,* vol. 394, p. 124881, 2020, doi: 10.1016/j.cej.2020.124881.
[26] S. Kyrimis, M. E. Potter, R. Raja, and L.-M. Armstrong, "Understanding catalytic CO2 and CO conversion into methanol using computational fluid dynamics," *Faraday Discussions,* 10.1039/D0FD00136H 2021, doi: 10.1039/D0FD00136H.
[27] F. Nestler *et al.*, "A novel approach for kinetic measurements in exothermic fixed bed reactors: advancements in non-isothermal bed conditions demonstrated for methanol synthesis," *Reaction Chemistry & Engineering,* 10.1039/D1RE00071C vol. 6, no. 6, pp. 1092-1107, 2021, doi: 10.1039/D1RE00071C.
[28] D. S. Kourkoumpas, E. Papadimou, K. Atsonios, S. Karellas, P. Grammelis, and E. Kakaras, "Implementation of the Power to Methanol concept by using CO2 from lignite power plants: Techno-economic investigation," *International Journal of Hydrogen Energy,* vol. 41, no. 38, pp. 16674-16687, 2016/10/15/ 2016, doi: https://doi.org/10.1016/j.ijhydene.2016.07.100.
[29] M. Pérez-Fortes, J. C. Schöneberger, A. Boulamanti, and E. Tzimas, "Methanol synthesis using captured CO2 as raw material: Techno-economic and environmental assessment," *Applied Energy,* vol. 161, pp. 718-732, 2016/01/01/ 2016, doi: https://doi.org/10.1016/j.apenergy.2015.07.067.
[30] C. Hank *et al.*, "Economics & carbon dioxide avoidance cost of methanol production based on renewable hydrogen and recycled carbon dioxide – power-to-methanol," *Sustainable*

Energy & Fuels, 10.1039/C8SE00032H vol. 2, no. 6, pp. 1244-1261, 2018, doi: 10.1039/C8SE00032H.

[31] S. Pratschner, F. Radosits, A. Ajanovic, and F. Winter, "Techno-economic assessment of a power-to-green methanol plant," *Journal of CO2 Utilization,* vol. 75, p. 102563, 2023/09/01/ 2023, doi: https://doi.org/10.1016/j.jcou.2023.102563.

[32] European Commission. "EU Emissions Trading System (EU ETS)." https://climate.ec.europa.eu/eu-action/eu-emissions-trading-system-eu-ets_en (accessed.

[33] World Bank. "Revenue generated by the European Union Emission Trading System (EU-ETS) from 2008 to 2022 (in million U.S. dollars)." https://www.statista.com/statistics/1326984/european-union-ets-revenue/ (accessed.

[34] F. Bisotti, M. Fedeli, K. Prifti, A. Galeazzi, A. Dell'Angelo, and F. Manenti, "Impact of Kinetic Models on Methanol Synthesis Reactor Predictions: In Silico Assessment and Comparison with Industrial Data," *Industrial & Engineering Chemistry Research,* vol. 61, no. 5, pp. 2206-2226, 2022/02/09 2022, doi: 10.1021/acs.iecr.1c04476.

[35] J. B. Hansen, "Methanol Production Technology: Todays and future Renewable solutions," in *Haldor Topsøe*, Lund University, 2015.

[36] V. Dieterich, A. Buttler, A. Hanel, H. Spliethoff, and S. Fendt, "Power-to-liquid via synthesis of methanol, DME or Fischer–Tropsch-fuels: a review," *Energy & Environmental Science,* 10.1039/D0EE01187H vol. 13, no. 10, pp. 3207-3252, 2020, doi: 10.1039/D0EE01187H.

[37] A. Pinto and P. L. Rogerson, "Impact of high fuel cost on plant design," *Chemengng Progress,* vol. 73, pp. 95-100, 1977.

[38] J. Haid and U. Koss, "Lurgi's Mega-Methanol technology opens the door for a new era in down-stream applications," in *Studies in Surface Science and Catalysis*, vol. 136, E. Iglesia, J. J. Spivey, and T. H. Fleisch Eds.: Elsevier, 2001, pp. 399-404.

[39] M. Bayat, M. R. Rahimpour, M. Taheri, M. Pashaei, and S. Sharifzadeh, "A comparative study of two different configurations for exothermic–endothermic heat exchanger reactor," *Chemical Engineering and Processing: Process Intensification,* vol. 52, pp. 63-73, 2012/02/01/ 2012, doi: https://doi.org/10.1016/j.cep.2011.11.010.

[40] S. Jamshidi, M. H. Sedaghat, A. Amini, and M. R. Rahimpour, "CFD simulation and sensitivity analysis of an industrial packed bed methanol synthesis reactor," *Chemical Engineering and Processing - Process Intensification,* vol. 183, p. 109244, 2023/01/01/ 2023, doi: https://doi.org/10.1016/j.cep.2022.109244.

[41] F. Keramat, A. Mirvakili, A. Shariati, and M. R. Rahimpour, "Investigation of anti-condensation strategies in the methanol synthesis reactor using computational fluid dynamics," *Korean Journal of Chemical Engineering,* vol. 38, no. 10, pp. 2020-2033, 2021/10/01 2021, doi: 10.1007/s11814-021-0916-z.

[42] A. Mirvakili, A. Bakhtyari, and M. R. Rahimpour, "A CFD modeling to investigate the impact of flow mal-distribution on the performance of industrial methanol synthesis reactor," *Applied Thermal Engineering,* vol. 128, pp. 64-78, 2018/01/05/ 2018, doi: https://doi.org/10.1016/j.applthermaleng.2017.08.145.

[43] A. Mirvakili and M. R. Rahimpour, "Mal-distribution of temperature in an industrial dual-bed reactor for conversion of CO2 to methanol," *Applied Thermal Engineering,* vol. 91, pp. 1059-1070, 2015/12/05/ 2015, doi: https://doi.org/10.1016/j.applthermaleng.2015.08.067.

[44] M. R. Rahimpour, S. Ghader, M. Baniadam, and J. Fathi Kalajahi, "Incorporation of Flexibility in the Design of a Methanol Synthesis Loop in the Presence of Catalyst Deactivation," *Chemical Engineering & Technology,* vol. 26, no. 6, pp. 672-678, 2003, doi: 10.1002/ceat.200390102.

[45] M. R. Rahimpour, F. Rahmani, M. Bayat, and E. Pourazadi, "Enhancement of simultaneous hydrogen production and methanol synthesis in thermally coupled double-membrane reactor," *International Journal of Hydrogen Energy,* vol. 36, no. 1, pp. 284-298, 2011/01/01/ 2011, doi: https://doi.org/10.1016/j.ijhydene.2010.09.074.

[46] B. Rahmatmand, M. R. Rahimpour, and P. Keshavarz, "Introducing a novel process to enhance the syngas conversion to methanol over Cu/ZnO/Al2O3 catalyst," *Fuel Processing Technology,* vol. 193, pp. 159-179, 2019/10/01/ 2019, doi: https://doi.org/10.1016/j.fuproc.2019.05.014.

[47] N. Rezaie, A. Jahanmiri, B. Moghtaderi, and M. R. Rahimpour, "A comparison of homogeneous and heterogeneous dynamic models for industrial methanol reactors in the presence of catalyst deactivation," *Chemical Engineering and Processing: Process Intensification,* vol. 44, no. 8, pp. 911-921, 2005, doi: 10.1016/j.cep.2004.10.004.

[48] F. Samimi, M. Feilizadeh, M. Ranjbaran, M. Arjmand, and M. R. Rahimpour, "Phase stability analysis on green methanol synthesis process from CO2 hydrogenation in water cooled, gas cooled and double cooled tubular reactors," *Fuel Processing Technology,* vol. 181, pp. 375-387, 2018/12/01/ 2018, doi: https://doi.org/10.1016/j.fuproc.2018.10.004.

[49] G. Zahedi, A. Elkamel, A. Lohi, A. Jahanmiri, and M. R. Rahimpor, "Hybrid artificial neural network—First principle model formulation for the unsteady state simulation and analysis of a packed bed reactor for CO2 hydrogenation to methanol," *Chemical Engineering Journal,* vol. 115, no. 1, pp. 113-120, 2005/12/15/ 2005, doi: https://doi.org/10.1016/j.cej.2005.08.018.

[50] H. Kordabadi and A. Jahanmiri, "Optimization of methanol synthesis reactor using genetic algorithms," *Chemical Engineering Journal,* vol. 108, no. 3, pp. 249-255, 2005/04/15/ 2005, doi: https://doi.org/10.1016/j.cej.2005.02.023.

[51] F. Manenti and G. Bozzano, "Optimal Control of Methanol Synthesis Fixed-Bed Reactor," *Industrial & Engineering Chemistry Research,* vol. 52, no. 36, pp. 13079-13091, 2013/09/11 2013, doi: 10.1021/ie401511e.

[52] A. Elkamel, G. Reza Zahedi, C. Marton, and A. Lohi, "Optimal Fixed Bed Reactor Network Configuration for the Efficient Recycling of CO2 into Methanol," *Energies*, vol. 2, no. 2*,* pp. 180-189doi: 10.3390/en20200180.

[53] S. Kyrimis, R. Raja, and L.-M. Armstrong, "Image processing of computed tomography scanned poly-dispersed beds for computational fluid dynamic studies," *Advanced Powder Technology (under review),* 2023.

[54] M. Zhang, H. Dong, and Z. Geng, "Computational study of particle packing process and fluid flow inside Polydisperse cylindrical particles fixed beds," *Powder Technology,* vol. 354, pp. 19-29, 2019/09/01/ 2019, doi: https://doi.org/10.1016/j.powtec.2019.05.061.

[55] G. Boccardo, F. Augier, Y. Haroun, D. Ferré, and D. L. Marchisio, "Validation of a novel open-source work-flow for the simulation of packed-bed reactors," *Chemical Engineering Journal,* vol. 279, pp. 809-820, 2015/11/01/ 2015, doi: https://doi.org/10.1016/j.cej.2015.05.032.

[56] F. Manenti, S. Cieri, and M. Restelli, "Considerations on the steady-state modeling of methanol synthesis fixed-bed reactor," *Chemical Engineering Science,* vol. 66, no. 2, pp. 152-162, 2011, doi: 10.1016/j.ces.2010.09.036.

[57] A. G. Dixon, M. Nijemeisland, and E. H. Stitt, "Packed Tubular Reactor Modeling and Catalyst Design using Computational Fluid Dynamics," *Computational Fluid Dynamics,* vol. 31, pp. 307-389, 2006, doi: 10.1016/s0065-2377(06)31005-8.

[58] G. D. Wehinger, T. Eppinger, and M. Kraume, "Detailed numerical simulations of catalytic fixed-bed reactors: Heterogeneous dry reforming of methane," *Chemical Engineering Science,* vol. 122, pp. 197-209, 2015, doi: 10.1016/j.ces.2014.09.007.

[59] A. G. Dixon and B. Partopour, "Computational Fluid Dynamics for Fixed Bed Reactor Design," *Annual Review of Chemical and Biomolecular Engineering,* vol. 11, no. 1, pp. 109-130, 2020, doi: 10.1146/annurev-chembioeng-092319-075328.

[60] B. Partopour and A. G. Dixon, "Computationally efficient incorporation of microkinetics into resolved-particle CFD simulations of fixed-bed reactors," vol. 88, pp. 126-134, 2016, doi: 10.1016/j.compchemeng.2016.02.015.

[61] S. Kyrimis, R. Robert, and L.-M. Armstrong, "Quantifying the impact of intraparticle convection within fixed beds formed by catalytic particles with low macro-porosities," *ACS Engineering Au (Under review),* 2023.
[62] A. G. Dixon, "Local transport and reaction rates in a fixed bed reactor tube: Endothermic steam methane reforming," *Chemical Engineering Science,* vol. 168, pp. 156-177, 2017, doi: 10.1016/j.ces.2017.04.039.
[63] A. G. Dixon, "Local transport and reaction rates in a fixed bed reactor tube: Exothermic partial oxidation of ethylene," *Chemical Engineering Science,* vol. 231, p. 116305, 2021/02/15/ 2021, doi: https://doi.org/10.1016/j.ces.2020.116305.
[64] B. Partopour and A. G. Dixon, "Integrated multiscale modeling of fixed bed reactors: Studying the reactor under dynamic reaction conditions," *Chemical Engineering Journal,* vol. 377, p. 119738, 2019/12/01/ 2019, doi: https://doi.org/10.1016/j.cej.2018.08.124.
[65] S. Kyrimis, K. E. Rankin, M. E. Potter, R. Raja, and L.-M. Armstrong, "Towards realistic characterisation of chemical reactors: An in-depth analysis of catalytic particle beds produced by sieving," *Advanced Powder Technology,* vol. 34, no. 2, p. 103932, 2023/02/01/ 2023, doi: https://doi.org/10.1016/j.apt.2022.103932.
[66] S. Kyrimis, Robert Raja, and L.-M. Armstrong, "Hydrodynamic profiles of computed tomography-scanned polydispersed beds produced by sieving," *Proceedings of the 10th International Conference on Fluid Flow, Heat and Mass Transfer (FFHMT '23),* 2023, doi: 10.11159/ffhmt23.171.
[67] Stylianos Kyrimis, Robert Raja, and L.-M. Armstrong, "Impact of Particle Size on the Selection of a Representative Bed Section for Poly-Dispersed Fixed Bed Reactors," *Journal of Fluid Flow, Heat and Mass Transfer (JFFHMT),* vol. 10, pp. 24-35, 2023, doi: 10.11159/jffhmt.2023.004.
[68] ANSYS Inc., "ANSYS Fluent Theory Guide," *Fluent Theory Guide,* vol. Release 15.0, November 2013 2013.
[69] ANSYS Inc., "ANSYS Fluent User's Guide," *Fluent User's Guide,* vol. Release 15.0, November 2013 2013.
[70] S. Ergun, "Fluid flow through packed columns," *Chem. Eng. Prog.,* vol. 48, pp. 89-94, 1952 1952. [Online]. Available: https://ci.nii.ac.jp/naid/10003393451/en/.
[71] T. Tosco, D. L. Marchisio, F. Lince, and R. Sethi, "Extension of the Darcy–Forchheimer Law for Shear-Thinning Fluids and Validation via Pore-Scale Flow Simulations," *Transport in Porous Media,* vol. 96, no. 1, pp. 1-20, 2013/01/01 2013, doi: 10.1007/s11242-012-0070-5.
[72] A. Montillet, E. Akkari, and J. Comiti, "About a correlating equation for predicting pressure drops through packed beds of spheres in a large range of Reynolds numbers," *Chemical Engineering and Processing: Process Intensification,* vol. 46, no. 4, pp. 329-333, 2007/04/01/ 2007, doi: https://doi.org/10.1016/j.cep.2006.07.002.
[73] E. Erdim, Ö. Akgiray, and İ. Demir, "A revisit of pressure drop-flow rate correlations for packed beds of spheres," *Powder Technology,* vol. 283, pp. 488-504, 2015/10/01/ 2015, doi: https://doi.org/10.1016/j.powtec.2015.06.017.
[74] A. G. Dixon, "General correlation for pressure drop through randomly-packed beds of spheres with negligible wall effects," *AIChE Journal,* vol. 69, no. 6, p. e18035, 2023/06/01 2023, doi: https://doi.org/10.1002/aic.18035.
[75] E. Achenbach, "Heat and flow characteristics of packed beds," *Experimental Thermal and Fluid Science,* vol. 10, no. 1, pp. 17-27, 1995, doi: 10.1016/0894-1777(94)00077-l.
[76] A. G. Dixon, "Correlations for wall and particle shape effects on fixed bed bulk voidage," *The Canadian Journal of Chemical Engineering,* https://doi.org/10.1002/cjce.5450660501 vol. 66, no. 5, pp. 705-708, 1988/10/01 1988, doi: https://doi.org/10.1002/cjce.5450660501.
[77] A. Guardo, M. Coussirat, M. A. Larrayoz, F. Recasens, and E. Egusquiza, "Influence of the turbulence model in CFD modeling of wall-to-fluid heat transfer in packed beds," *Chemical*

Engineering Science, vol. 60, no. 6, pp. 1733-1742, 2005/03/01/ 2005, doi: https://doi.org/10.1016/j.ces.2004.10.034.

[78] A. G. Dixon, M. Ertan Taskin, M. Nijemeisland, and E. H. Stitt, "Systematic mesh development for 3D CFD simulation of fixed beds: Single sphere study," *Computers & Chemical Engineering,* vol. 35, no. 7, pp. 1171-1185, 2011/07/11/ 2011, doi: https://doi.org/10.1016/j.compchemeng.2010.12.006.

[79] R. H. Hite and R. Jackson, "Pressure gradients in porous catalyst pellets in the intermediate diffusion regime," *Chemical Engineering Science,* vol. 32, no. 7, pp. 703-709, 1977/01/01/ 1977, doi: https://doi.org/10.1016/0009-2509(77)80117-6.

[80] V. Spallina, B. Marinello, F. Gallucci, M. C. Romano, and M. Van Sint Annaland, "Chemical looping reforming in packed-bed reactors: Modelling, experimental validation and large-scale reactor design," *Fuel Processing Technology,* vol. 156, pp. 156-170, 2017/02/01/ 2017, doi: https://doi.org/10.1016/j.fuproc.2016.10.014.

[81] S. H. Fogler, *Elements of Chemical Reaction Engineering, 5th Edition*. Pearson, 2016.

[82] C.-T. Lin and T. E. Daubert, "Estimation of Partial Molar Volume and Fugacity Coefficient of Components in Mixtures from the Soave and Peng-Robinson Equations of State," *Industrial & Engineering Chemistry Process Design and Development,* vol. 19, no. 1, pp. 51-59, 1980/01/01 1980, doi: 10.1021/i260073a009.

[83] ANSYS Inc., "DesignXplorer User's Guide," *Release 2021 R2,* 2021.

[84] B. Partopour and A. G. Dixon, "An integrated workflow for resolved-particle packed bed models with complex particle shapes," *Powder Technology,* vol. 322, pp. 258-272, 2017/12/01/ 2017, doi: https://doi.org/10.1016/j.powtec.2017.09.009.

[85] G. D. Wehinger, C. Fütterer, and M. Kraume, "Contact Modifications for CFD Simulations of Fixed-Bed Reactors: Cylindrical Particles," *Industrial & Engineering Chemistry Research,* vol. 56, no. 1, pp. 87-99, 2017/01/11 2017, doi: 10.1021/acs.iecr.6b03596.

[86] S. J. Rodrigues, N. Vorhauer-Huget, T. Richter, and E. Tsotsas, "Influence of Particle Shape on Tortuosity of Non-Spherical Particle Packed Beds," *Processes,* vol. 11, no. 1, p. 3, 2023. [Online]. Available: https://www.mdpi.com/2227-9717/11/1/3.

[87] S. J. Rodrigues, N. Vorhauer-Huget, and E. Tsotsas, "Prediction of effective thermal conductivity of packed beds of polyhedral particles," *Powder Technology,* vol. 430, p. 118997, 2023/12/01/ 2023, doi: https://doi.org/10.1016/j.powtec.2023.118997.

[88] M. Marek and P. Niegodajew, "Experimental analysis of the orientation distribution of cylindrical particles with different aspect ratios in random packed beds," *Advanced Powder Technology,* vol. 34, no. 11, p. 104206, 2023/11/01/ 2023, doi: https://doi.org/10.1016/j.apt.2023.104206.

[89] P. Niegodajew, K. Gruszka, and M. Marek, "Numerical study of cylindrical particles' orientation in narrow packed beds," *Powder Technology,* vol. 386, pp. 528-539, 2021/07/01/ 2021, doi: https://doi.org/10.1016/j.powtec.2021.03.069.

[90] ACS. "Endangered Elements." https://www.acs.org/greenchemistry/research-innovation/endangered-elements.html (accessed.